The STA1–DOT2 interaction promotes nuclear speckle formation and splicing robustness in growth and heat stress responses

Heejin Kim[1], Kyoung-jae Yu[1], So Young Park[2], Dong Hye Seo[3, 4, 5], Dong-Hoon Jeong[2], Woo Taek Kim[5], Dae-Jin Yun[6], and Byeong-ha Lee[1*]

[1]Department of Life Science, Sogang University, Mapo-gu, Seoul 04107, Republic of Korea

[2]Department of Life Science and and Multidisciplinary Genome Institute, Hallym University, Chuncheon 24252, Republic of Korea

[3]Plant Biotechnology Research Center, Ghent University, Global Campus, Incheon 21985, Republic of Korea

[4]Department of Plant Biotechnology and Bioinformatics, Ghent University, 9052 Ghent, Belgium

[5]Department of Systems Biology and Institute of Life Science and Biotechnology, Yonsei University, Seoul 03722, Republic of Korea

[6]Department of Advanced Biotechnology and Global Plant Stress Research Center, Konkuk University, 05029, Seoul, Republic of Korea

Contact information

Heejin Kim: gmlwls7686@sogang.ac.kr / 0009-0000-2341-5581

Kyoung-jae Yu: kyoungjae@sogang.ac.kr / 0009-0003-1125-572X

Dong Hye Seo: Donghye.Seo@ghent.ac.kr / 0000-0003-1243-4466

So Young Park: soyoungp@hallym.ac.kr / 0000-0001-9202-0874

Dong-Hoon Jeong: dhjeong73@hallym.ac.kr / 0000-0002-2378-1706

Woo Taek Kim: wtkim@yonsei.ac.kr / 0000-0001-5027-4622

Dae-Jin Yun: djyun@konkuk.ac.kr / 0000-0002-3638-6043

*Correspondence: Byeong-ha Lee: byeongha@sogang.ac.kr / 0000-0001-7633-3264

ABSTRACT

Pre-mRNA splicing is carried out by the spliceosome, a large and dynamic ribonucleoprotein complex. The spliceosome is known to be stored in nuclear speckles (NS), which are now recognized as active subnuclear organelles for splicing. However, it remains poorly understood how spliceosomal protein-protein interactions are functionally coupled to NS organization to maintain splicing robustness in plants. Here, we report the functional significance of a specific interaction between two U4/U6·U5 tri-snRNP components of the spliceosome, STA1 and DOT2, in regulating NS organization, pre-mRNA splicing, and heat stress responses in *Arabidopsis*. We identified a missense mutation in DOT2 (a Snu66/SART1 homolog) from a genetic suppressor of the PRP6 homolog mutant *sta1-1* (named *S307*). This mutation restored the weakened interaction between STA1 and DOT2 in the *sta1-1* mutant background. Genetic, biochemical, and cell biological analyses showed that variation in the strength of the STA1-DOT2 interaction was closely associated with changes in NS formation, splicing efficiency, as well as growth and heat tolerance. Pharmacological inhibition of STA1-associated NS formation by tubercidin recapitulated *sta1-1*-like phenotypes and splicing defects, supporting a functional link between NS organization and splicing outcomes. In addition, heat-induced weakening of the STA1-DOT2 interaction was accompanied by reduced NS formation and increased intron retention at the transcriptome-wide level including key heat-responsive transcripts. Based on these observations, we propose that the STA1-DOT2 interaction, likely reflecting the assembly state of the U4/U6·U5 tri-snRNP, functions as a heat-sensitive interaction node that couples spliceosome assembly to NS organization and splicing robustness under stress conditions.

Keywords: *STA1*, *DOT2*, U4/U6·U5 tri-snRNP, spliceosomal protein interaction, splicing, nuclear speckle

55 **INTRODUCTION**

56 Pre-mRNA splicing is an essential step in eukaryotic gene expression and is carried
57 out by the spliceosome, a large and dynamic ribonucleoprotein complex composed of five
58 small nuclear ribonucleoproteins (snRNPs) and numerous auxiliary factors (Will and
59 Lührmann, 2011). Among spliceosomal subcomplexes, the U4/U6·U5 tri-snRNP plays a
60 pivotal role in spliceosome activation, and undergoes extensive structural rearrangements
61 during the splicing cycle (Sander et al., 2006; Will and Lührmann, 2011). Defects in tri-snRNP
62 assembly or stability result in splicing failure, underscoring the importance of precise and
63 coordinated interactions among its components (Klimesová et al., 2021; Schneider et al., 2010).

64 *Arabidopsis* STABILIZED1 (STA1) is homologous to the pre-mRNA splicing factors
65 PRP1, Prp6p, and PRPF6 (hereafter collectively referred to as PRP6, unless otherwise indicated)
66 in *Schizosaccharomyces pombe*, *Saccharomyces cerevisiae*, and *Homo sapiens*, respectively.
67 Within the tri-snRNP, PRP6 resides in the U5 snRNP and interacts with components of the
68 U4/U6 di-snRNP, thereby physically bridging the U5 snRNP and the U4/U6 di-snRNP
69 (Bertram et al., 2017; Liu et al., 2006; Makarov et al., 2000; Nguyen et al., 2016; Zhan et al.,
70 2018). Consistent with this role, depletion or mutation of PRP6 in yeast and human cells
71 disrupts tri-snRNP formation and leads to the accumulation of U4/U6 di-snRNP, indicating
72 that PRP6 is essential for tri-snRNP assembly (Galisson and Legrain, 1993; Schaffert et al.,
73 2004).

74 The *Arabidopsis sta1-1* mutant carries a 6-bp deletion within the half-a-
75 tetratricopeptide (HAT) repeat domain of STA1 (Lee et al., 2006). HAT domains are known to
76 mediate protein–protein interactions and promote the assembly of multiprotein complexes
77 (Zeytuni and Zarivach, 2012). Supporting this, yeast two-hybrid assays using human tri-snRNP
78 components have shown that PRPF6 interacts with several tri-snRNP components through its
79 HAT domain (Liu *et al.*, 2006). These findings suggest that the PRP6 homolog STA1
80 contributes to pre-mRNA splicing in plants primarily by promoting proper spliceosome
81 assembly through its interactions with other tri-snRNP components.

82 In the nucleus, nuclear speckles (NS) are prominent subnuclear membraneless
83 compartments enriched in spliceosomal proteins and RNAs (Ilik et al., 2020; Smith et al., 2020).
84 NS serve as sites for the storage, assembly, and dynamic exchange of splicing factors and are
85 closely associated with transcriptionally active chromatin, and are increasingly recognized as
86 sites that actively contribute to efficient pre-mRNA processing (Daguenet et al., 2012; Wu et
87 al., 2024). NS are thought to form through the self-assembly of resident proteins and RNAs
88 and to be maintained by transient protein-protein and protein-RNA interactions (Choi et al.,
89 2025; Day et al., 2012; Kim et al., 2016; Paul et al., 2024). Importantly, localization of
90 spliceosomal components to NS enhances the splicing efficiency of nearby genes, whereas
91 impaired speckle association leads to splicing defects (Liu et al., 2021; Wang et al., 2024).

92 Several lines of evidence suggest that tri-snRNP components contribute directly to NS
93 organization. In human cells, depletion of PRPF6 disrupts the NS localization of another tri-
94 snRNP component PRPF31 and causes splicing defects (Yildirim et al., 2021). In plants, NS
95 localization of splicing factors has also been implicated in stress adaptation. For example, two
96 alternatively spliced isoforms of RDM16 (a tri-snRNP component PRPF3 homolog)
97 cooperatively promote nuclear condensation and enhance heat tolerance in *Arabidopsis* (Ma et
98 al., 2025). These studies support the idea that NS organization is functionally linked to
99 spliceosome integrity and splicing outcomes, particularly under stress. However, it remains
100 unclear how the interaction-dependent assembly state of the tri-snRNP contributes to NS
101 organization in plants.

102 In this study, from a *sta1-1* suppressor line (*S307*), we identified a missense mutation
103 in DOT2 ($dot2^S$), a U4/U6·U5 tri-snRNP component homologous to yeast Snu66p and human
104 SART1, which are known to bind to and stabilize the PRP6-involved bridge within the tri-
105 snRNP (Bertram *et al.*, 2017; Zhan *et al.*, 2018). The $dot2^S$ suppressor allele restores the
106 weakened interaction between STA1 and DOT2 in the *sta1-1* background, leading to recovery
107 of NS formation, improved pre-mRNA splicing, and restoration of growth and heat tolerance.
108 Our results support the idea that the STA1-DOT2 interaction functions as a critical and heat-
109 sensitive interaction node within the tri-snRNP, contributing to spliceosome assembly to NS
110 organization, and splicing robustness under stress conditions.

RESULTS

A mutation in *DOT2*, a U4/U6·U5 tri-snRNP-associated protein, suppresses the *sta1-1* defects

The *sta1-1* mutants are small in size and hypersensitive to heat (Kim et al., 2017; Lee *et al.*, 2006). To elucidate the molecular mechanism behind it, we employed a forward genetic approach to identify *sta1-1* modifiers, which could reveal the genetic interactors of *STA1*. From an ethyl methanesulfonate (EMS)-treated *sta1-1* mutant pool, we isolated a *sta1-1* suppressor *S307* based on its size recovery. *S307* suppressed the small size phenotype of *sta1-1*, exhibiting the phenotype similar to wild-type (WT, Columbia harboring a *RD29A* promoter-driven luciferase transgene) (Figure 1A). In addition to the restored size, the splicing defects observed in *sta1-1* were also restored to wild-type levels in *S307* (Figures 1B and 1C). Intron retention (IR) profiles of *S307* were more similar to those of WT rather than to those of *sta1-1*, as shown by heatmaps (Figure 1B). Only 16 transcripts (16 increased, 0 decreased) displayed differential IR between *S307* and WT, in contrast to 2,876 transcripts (2,860 increased, 16 decreased) between s*ta1-1* and WT (Figure 1C, Supplemental Table 2).

Whole-genome sequencing combined with map-based positional cloning, using the F2 suppressor seedlings from a cross between *S307* and Landsberg *erecta* identified a G-to-A point mutation in the 8th exon of the *DEFECTIVELY ORGANIZED TRIBUTARIES 2* (*DOT2*, At5g16780) gene (herein, called *dot2*^{S}). This mutation results in an amino acid change from aspartate to asparagine (Supplemental Figure 1). The *DOT2* gene encodes a protein homologous to Snu66p in *Saccharomyces cerevisiae* and SART1 in *Homo sapiens*, both of which are components of the U4/U6·U5 tri-snRNP (Supplemental Figure 2A) together with STA1. Indeed, *DOT2* promoter-driven GUS activity was detected across all tissues, as found in the *STA1::GUS* plants (Lee et al., 2006) (Supplemental Figure 2B). This widespread and overlapping expression pattern suggests constant and cooperative roles for DOT2 and STA1.

To further examine whether DOT2 functions together with STA1, we characterized two independent *dot2* single mutant alleles: a *dot2* single mutant carrying the *S307* allele and a *dot2* T-DNA insertion mutant (SAIL_775_F10, also known as *mdf-2*) (de Luxan-Hernandez et al., 2022), hereafter referred to as *dot2*^{S} and *dot2*^{T}, respectively. *dot2*^{S} plants were comparable to WT in both growth and splicing patterns, whereas *dot2*^{T} plants showed growth and splicing

defects resembling those of *sta1-1* (Supplemental Figure 3A and 3B). Consistent with previous reports (de Luxan-Hernandez *et al.*, 2022), *dot2*^{T} plants displayed cell death in the root apical meristem (RAM) as revealed by propidium iodide (PI)-stained confocal imaging. However, no detectable RAM defects were observed in the *dot2*^{S} plants (Supplemental Figure 3C). Together, these results indicate that *dot2*^{S} represents a weak loss-of-function allele and that *dot2* loss-of-function mutants display *sta1-1*-like defects, suggesting a coordinated function for DOT2 and STA1 in growth and pre-mRNA splicing.

Genetic and molecular assays confirm *dot2*^{S} as a semi-dominant suppressor of *sta1-1*

To confirm that the *dot2*^{S} mutation is the causal mutation, a genomic fragment of *DOT2* including its endogenous promoter was introduced into *S307* via *Agrobacterium*-mediated transformation. Unexpectedly, transgenic plants expressing this genomic fragment of *DOT2* (*S307*^{DOT2END}) did not revert the WT-like phenotype of *S307* to the small-sized *sta1-1* phenotypes (Figure 1D). However, when the *DOT2* gene was overexpressed by the Cauliflower Mosaic Virus (CaMV) 35S promoter in *S307* (*S307*^{DOT2OX}), the overexpressing plants exhibited the *sta1-1*-like small size (Figure 1D). In addition, compared to *S307*^{DOT2END}, *S307*^{DOT2OX} exhibited higher accumulation of intron-retained transcripts for several marker genes that show IR in *sta1-1*, showing stronger phenotypic reversion by the overexpression (Figure 1E). We speculated that phenotypic reversion only by *DOT2* overexpression might be due to the dominant or semi-dominant effects of the dot2^{S} mutant protein on sta1-1, relative to those of the wild-type DOT2 protein; the dot2^{S} protein may interact more effectively with the sta1-1 protein than the DOT2 protein. Thus, we performed a dominance test on *dot2*^{S} by genetically combining *dot2*^{S} with the *STA1* homozygotes (WT) or the *sta1-1* homozygotes. While no clear size defects were observed in the combinations of *dot2*^{S} mutation in the wild-type background, the *dot2*^{S} heterozygote in the *sta1-1* background showed an intermediate size, supporting the notion of semi-dominant effects of dot2^{S} on sta1-1 (Figure 1F). Consistently, the *dot2*^{S} heterozygote in the *sta1-1* background exhibited intermediate levels of splicing defects between the *DOT2* (i.e., *sta1-1*) and the *dot2*^{S} homozygotes in *sta1-1* (i.e., *S307*) (Figure 1G). Taken together, these results confirm that the mutation in *DOT2* is responsible for the *sta1-1* phenotypic suppression in *S307*.

171 **The *dot2^S* mutation restores physical interaction with sta1-1, rescuing *sta1-1* defects**

172 Homologs of STA1 and DOT2 are known to interact, as supported by structural and
173 experimental evidence (Häcker et al., 2008; Liu *et al.*, 2006; Sun et al., 2018; Zhan *et al.*, 2018).
174 Our genetic data suggested that STA1 and DOT2 likely interact physically. In support of this,
175 our structural modeling predicted an interaction between *Arabidopsis* STA1 and DOT2, with
176 the *sta1-1* and *dot2^S* mutations positioned near the predicted interface (Supplemental Figure
177 4A). The *sta1-1* mutation resides within the HAT domain, which mediates protein-protein
178 interactions (Zeytuni and Zarivach, 2012), and the *dot2^S* mutation maps to the predicted STA1-
179 interacting surface identified by InterProSurf and PDBePISA (Krissinel and Henrick, 2007;
180 Negi et al., 2007) (Supplemental Figure 4B). These findings suggest that both mutations may
181 alter the STA1-DOT2 interaction. We examined interactions between the wild type and mutant
182 proteins using yeast two-hybrid (Y2H) assays. As expected, STA1 and DOT2 showed
183 substantial interaction (Figure 1H), whereas interactions between a wild-type protein (STA1 or
184 DOT2) and a mutant protein (sta1-1 or dot2^S) were not detectable. Interestingly, and consistent
185 with our expectation, sta1-1 and dot2^S showed interactions comparable to those between STA1
186 and DOT2 (Figure 1H). Consistent with these observations, bimolecular fluorescence
187 complementation (BiFC) analysis further confirmed the sta1-1-dot2^S interaction similar to the
188 STA1-DOT2 interaction (Figure 1I and 1J).

189 To determine whether the suppressive effect is allele-specific, we generated an
190 additional *dot2* allele using CRISPR/Cas9 (herein, called *dot2^C*). The *dot2^C* mutation is a 3-bp
191 deletion located 44 bp upstream of the *dot2^S* mutation, outside the predicted STA1-DOT2
192 interaction interface (Supplemental Figure 4A-4C). Unlike dot2^S, the dot2^C protein did not alter
193 interaction strength with STA1 or sta1-1 proteins (Figure 1I and 1J). Consistent with this, *dot2^C*
194 mutation did not alter the defects in size or intron retention observed in *sta1-1* (Supplemental
195 Figure 4D and 4E). These results indicate that *dot2^S* is a specific suppressor allele whose
196 product interacts with the sta1-1 mutant protein, thereby likely restoring the U4/U6·U5 tri-
197 snRNP assembly in *S307*.

198

199 **Interaction between STA1 and DOT2 promotes NS formation**

200 We noticed diverse nuclear localization signals in our BiFC assays. Thus, we examined
201 the localization of each GFP-tagged protein (STA1/sta1-1 and DOT2/dot2^{S}/dot2^{C}) and
202 classified nuclear signals into five subclasses depending on their subcompartments (Figure 2A).
203 Our observation revealed that STA1-GFP formed nuclear condensates (Class IV and V) at a
204 higher frequency than sta1-1-GFP, whereas GFP-DOT2/dot2^{S}/dot2^{C} were mainly distributed
205 throughout the nucleoplasm and nucleolus (Class II) (Figure 2B). Interestingly, co-expression
206 of STA1-GFP and mRFP-DOT2 significantly increased condensate formation of both proteins
207 compared to expression of each protein alone (from ~20%/0% to ~90% for STA1/DOT2)
208 (Figure 2C-2E). This suggests that the STA1-DOT2 interaction contributes to the localization
209 of each protein to nuclear condensates. This idea is supported by the following observations:
210 sta1-1-GFP showed limited condensate formation when co-expressed with mRFP-DOT2/dot2^{C},
211 whereas mRFP-dot2^{S} strongly enhanced sta1-1-GFP condensate formation (Figure 2C-2E),
212 consistent with the interaction strengths of these protein combinations. To identify the nature
213 of the nuclear condensates observed above, we co-expressed each protein with the NS marker
214 mRFP-U1-70K. STA1-GFP condensates showed partial co-localization with mRFP-U1-70K
215 (Figure 2F), whereas the EYFP signals from the BiFC assay, indicating the STA1-DOT2
216 interaction, showed complete co-localization with mRFP-U1-70K (Figure 2G). In addition, the
217 partial co-localization of STA1-GFP with mRFP-U1-70K became nearly complete in the
218 presence of DOT2 (Figure 2H). These results reconfirm that the STA1-DOT2 interaction
219 promotes nuclear condensate formation and reveal that the condensates correspond to NS. NS
220 are a specific type of nuclear condensates that are enriched in the spliceosome components and
221 associated with mRNA splicing and mRNA metabolism (Bhat et al., 2024; Daguenet *et al.*,
222 2012). Therefore, our results indicate that the STA1-DOT2 interaction contributes to their NS
223 formation and probably to proper mRNA splicing. It should be noted that STA1-GFP
224 condensates that did not overlap with mRFP-U1-70K suggest that STA1-GFP may form non-
225 functional or non-speckle-like condensates (herein called "aggregates") (see below).

226

227 **The *dot2^{S}* mutation restores sta1-1 localization to NS, enabling proper splicing**

228 We next examined the functional significance of NS formation of STA1 and DOT2 for
229 mRNA splicing. To this end, we generated the STA1-GFP/sta1-1-GFP overexpressing plants

230 in *Salk007933*, a *sta1* T-DNA insertion knock-out line (each named *Salk007933*$^{STA1\text{-}GFP}$ and
231 *Salk007933*$^{sta1\text{-}1\text{-}GFP}$). The homozygous *sta1* knockouts are lethal. However, introduction of
232 either STA1-GFP or sta1-1-GFP rescued this lethality and the resulting plants phenocopied the
233 wild-type and *sta1-1* plants, respectively (Supplemental Figure 5). Using protoplasts isolated
234 from these GFP-expressing plants, we also confirmed that the interaction between STA1 and
235 DOT2 (or sta1-1 and dot2^{S}) promoted the localization of the GFP-tagged protein to NS (Figure
236 3A). Previously, we developed a protoplast-based splicing activity assay using a luciferase
237 reporter gene fused with a genomic fragment of *HSFA3* (*gHSFA3-LUC*) which undergoes
238 STA1-dependent splicing (Kim *et al.*, 2017). After transfection of the alleles to be tested,
239 splicing activity was measured using protoplasts from *Salk007933*$^{sta1\text{-}1\text{-}GFP}$. As expected, the
240 introduction of STA1 into the protoplasts successfully restored full splicing activity of *gHSFA3-*
241 *LUC*, while sta1-1 did not (Figure 3B). Among the tested DOT2 alleles, only the dot2^{S} allele
242 showed the full splicing activity in *Salk007933*$^{sta1\text{-}1\text{-}GFP}$ (Figure 3B). Taken together, these
243 results indicate that the STA1-DOT2 or sta1-1-dot2^{S} interaction is critical for NS formation
244 and splicing activity, thereby linking NS formation to proper splicing activity.

245 We then examined the effect of disrupting NS formation by applying tubercidin, an
246 inhibitor of speckle formation (Kurogi et al., 2014) to *Salk007933*$^{STA1\text{-}GFP}$ plants. STA1-GFP in
247 *Salk007933*$^{STA1\text{-}GFP}$ is localized predominantly to NS (Figure 3C). However, tubercidin
248 treatment dispersed the GFP signals into the nucleoplasm (Figure 3C). Tubercidin treatment
249 also eliminated the differences in splicing activity and growth patterns among WT, *sta1-1*, and
250 *S307*, resulting in comparable splicing and growth phenotypes across all genotypes (Figure 3D
251 and 3E). Altogether, these results demonstrate that the interaction-dependent localization of
252 STA1 and DOT2 is functionally critical for proper mRNA splicing and that the *S307* suppressor
253 phenotypes are due to the rescued interaction between sta1-1 and dot2^{S}.

254

255 **Heat-induced weakening of the STA1–DOT2 interaction reduces nuclear speckle**
256 **formation**

257 To further assess the functional connection between the STA1-DOT2 interaction and
258 speckle formation, we employed heat as an additional perturbation to weaken protein-protein

interactions, because elevated temperatures can weaken molecular interactions. We also hypothesized that the heat-hypersensitive phenotype of *sta1-1* might result from heat-induced weakening of the sta1-1 interaction. Consistent with this idea, BiFC analysis revealed a reduction in EYFP signals corresponding to the STA1-DOT2 interaction after heat treatment (Figure 4A-4C).

Unexpectedly, despite the reduction in BiFC signals, heat treatment increased the numbers of STA1-GFP condensates when STA1-GFP was expressed alone (Supplemental Figure 6A). We hypothesized that the increase of heat-induced condensates might result from STA1 self-interaction (i.e., STA1 aggregation). To test this possibility, we performed BiFC analysis using STA1-nEYFP and STA1-cEYFP. Heat treatment indeed increased BiFC signals, indicating enhanced STA1 self-interaction under heat (Supplemental Figure 6B). Most EYFP signals derived from STA1 self-interaction did not overlap with signals from the speckle marker mRFP-U1-70K under either normal or heat conditions (Supplemental Figure 6C and 6D), suggesting that the STA1 self-interacting condensates are STA1 aggregates. This idea is further supported by the presence of a predicted intrinsically disordered regions (IDRs) within STA1 (residues 109-216, 298-318, 910-918, and 1022-1029), as identified by MolPhase (Liang et al., 2024) (Supplemental Figure 6E). Therefore, the increase of STA1-GFP condensates observed under the STA1-GFP single expression is likely the result of enhanced STA1-GFP self-aggregation.

To distinguish the NS from STA1 aggregates, we used BiFC analysis to quantify NS induced by the STA1-DOT2 interaction. The number of these speckle-representing BiFC signals in nuclei decreased after heat treatment and speckle formation was reduced in combinations of the weakly interacting STA1 and DOT2 allele products (Figures 4D-4G). These results reaffirm that the STA1-DOT2 interaction is required for efficient NS formation.

The *dot2*^{S} mutation suppresses the heat sensitivity of *sta1-1*

Next, we sought to determine whether the strength of the STA1-DOT2 interaction also plays an important role in the heat responses. The *sta1-1* mutants have previously been shown to display heat-sensitive phenotypes (Kim *et al.*, 2017; Kim et al., 2018). At both the seedling

288 and reproductive stages, the heat-sensitive phenotypes of *sta1-1* were almost fully rescued in
289 *S307* (Figure 5A–5C). These results along with the partial or full reversion to *sta1-1* heat
290 sensitivity observed in $S307^{DOT2OX}$ indicated that DOT2 functions together with STA1 under
291 heat stress (Figure 5A and 5C). In addition, the $dot2^{C}$ allele did not suppress the heat sensitivity
292 of s*ta1-1*, supporting the allele-specific suppressive effect of $dot2^{S}$ (Figure 5B and 5C). These
293 findings also suggest that the restored heat tolerance in *S307* results from the rescued
294 interaction between sta1-1 and $dot2^{S}$.

295

296 **The $dot2^{S}$ mutation mitigates transcriptome-wide intron retention defects in *sta1-1* under**
297 **heat stress**

298 Under heat stress, IR profiles in *S307* were partially restored toward WT levels (Figure
299 6A). Although the global splicing patterns in *S307* did not fully return to wild-type levels, the
300 IR defects of *sta1-1* were markedly improved in *S307*. Among 67,103 transcripts with
301 significant IR changes across genotypes, *S307* showed a reduced median IR ratio (0.14)
302 compared with *sta1-1* (0.34) (Figure 6B). Across the three genotypes under heat, 1,114 introns
303 (from 940 genes) showed increased IR in WT, whereas 58,522 introns (12,140 genes) and
304 36,617 introns (10,654 genes) showed increased IR in *sta1-1* and *S307*, respectively (Figure
305 6C, Supplemental Table 3). Venn diagram analysis further revealed that 27,514 introns with
306 elevated IR in *sta1-1* did not show increased IR in *S307* (Figure 6D).

307 Among the genes with restored splicing patterns, *HEAT SHOCK TRANSCRIPTION*
308 *FACTOR A1*s (*HSFA1*s), key upstream regulators of heat-responsive genes (Li et al., 2023;
309 Nishizawa-Yokoi et al., 2011; Röth et al., 2017), showed reduced intron retention in *S307*
310 compared with *sta1-1* (Figure 6E, Supplemental Figure 7). This recovery was further supported
311 by decreased levels of spliced transcripts and increased levels of intron-retained transcripts of
312 *HSFA1*s in $S307^{DOT2END}$ and $S307^{DOT2OX}$ relative to *S307* (Figure 6F). The $dot2^{C}$ allele failed to
313 rescue splicing defects of *HSFA1s* in *sta1-1*, consistent with its heat-sensitive phenotypes
314 (Figure 5B and 5C, Supplemental Figure 8). Proper splicing of *HSFA1s* in *S307* enabled normal
315 expression of downstream heat-responsive genes (Figure 6G). These findings indicate that
316 $dot2^{S}$ suppresses intron retention defects in heat-responsive genes in *sta1-1*, thereby

317 contributing to the restoration of heat tolerance. Taken together with the previous results, these
318 findings highlight the importance of the STA1-DOT2 interaction for proper heat stress
319 responses through NS formation and accurate mRNA splicing under heat conditions. It should
320 be noted that a partial rescue of splicing defects and heat sensitivity in *sta1-1*, particularly at
321 the pollen stage, under heat stress indicates that the sta1-1-dot2^{S} interaction is weaker than the
322 original STA1-DOT2 interaction.

323 **DISCUSSION**

324 Nuclear speckles (NS) are dynamic, membraneless nuclear compartments enriched in
325 spliceosomal components and RNAs (Mintz et al., 1999; Smith *et al.*, 2020), and are
326 increasingly recognized as active hubs that facilitate efficient pre-mRNA processing rather than
327 acting merely as passive storage sites (Wu *et al.*, 2024). Previous studies have emphasized the
328 contribution of intrinsically disordered regions, low-complexity domains, and multivalent
329 RNA–protein interactions to NS organization (Ku et al., 2025; Paul *et al.*, 2024; Wang *et al.*,
330 2024; Zhang et al., 2024). To what extent spliceosomal protein-protein interactions involved
331 in spliceosome assembly contribute to NS formation remains poorly understood. In this study,
332 we provide evidence that NS organization in plants is tightly associated with the integrity of a
333 specific interaction between two core U4/U6·U5 tri-snRNP components, STA1 and DOT2,
334 thereby linking spliceosome assembly with subnuclear organelle organization.

335 Our genetic and cell biological analyses show that the weakening of the STA1-DOT2
336 interaction by the *sta1-1* mutation is accompanied by reduced NS formation, compromised
337 splicing efficiency, and growth defects, whereas restoration of this interaction by the *dot2*^{S}
338 suppressor allele is associated with recovery of these phenotypes. Importantly, this suppression
339 is achieved through reinforcement of the STA1-DOT2 interaction probably within the tri-
340 snRNP. These observations suggest that NS organization is not independent of spliceosome
341 assembly status and is closely linked to the stability of specific spliceosomal interactions.

342 The spliceosome is a highly dynamic macromolecular complex, and formation of the
343 U4/U6·U5 tri-snRNP represents a critical step in each splicing cycle (Will and Lührmann,
344 2011). PRP6/STA1 functions as a central bridging factor between the U4/U6 di-snRNP and the
345 U5 snRNP, with its interactions stabilized by tri-snRNP–specific proteins such as
346 SART1/DOT2 (Bertram *et al.*, 2017; Nguyen *et al.*, 2016). Our observation of a positive
347 correlation between STA1–DOT2 interaction strength and NS abundance supports a model in
348 which proper tri-snRNP assembly facilitates efficient recruitment or retention of mature
349 spliceosomal complexes within NS. Consistent with this view, quantitative subnuclear
350 localization analyses revealed that co-expression of STA1-GFP and mRFP-DOT2 significantly
351 increased NS formation (types IV and V), compared with expression of each protein alone

352 (Figure 2B and 2D). In contrast, co-expression of sta1-1-GFP and mRFP-DOT2 resulted in
353 reduced NS-associated localization patterns (types IV and V) and increased localization to
354 Cajal bodies (type III) compared with the wild-type protein (Figure 2D). Tri-snRNPs are
355 assembled in Cajal bodies and subsequently redistributed to NS, which contain high levels of
356 mature, splicing-competent complexes (Schaffert *et al.*, 2004; Yildirim *et al.*, 2021). Thus, our
357 results suggest that the *sta1-1* mutation impairs later steps associated with NS organization due
358 to defects in the STA1-DOT2 interaction, likely leading to impaired formation of splicing-
359 competent spliceosome. In agreement with our results and speculation, when SART1,
360 homologous to DOT2, was immunologically depleted from HeLa cells, pre-mRNA splicing
361 was inhibited but the integrity of the U4/U6·U5 tri-snRNP was not affected, indicating the
362 importance of SART1 in active spliceosome formation and recruitment of the tri-snRNP to the
363 pre-spliceosome (Makarova et al., 2001; Utans et al., 1992). Thus, the STA1–DOT2 interaction
364 is likely to promote DOT2-dependent localization of STA1 to NS, concomitant with the
365 delivery of the tri-snRNP to the pre-spliceosome for active spliceosome assembly.

366 The functional relevance of our notion becomes particularly apparent under heat stress
367 conditions. Elevated temperatures are known to destabilize spliceosomal assemblies and
368 broadly impair splicing fidelity (Bond, 1988; Bond and James, 2000; Park et al., 2024). The
369 most sensitive component of the spliceosome is the U4/U6·U5 tri-snRNP (Bond, 1988). In this
370 context, the STA1–DOT2 interaction appears to function as a heat-sensitive interaction node,
371 since the heat-induced weakening of this interaction correlates with reduced NS formation,
372 increased intron retention, and weakened heat tolerance (Figure 4, Figure 5, Figure 6).
373 Reinforcement of the interaction by the dot2^{S} allele in sta1-1 (i.e., the *S307* suppressor) is
374 associated with improved NS formation and splicing performance, as well as partial recovery
375 of survival under heat stress (Figure 4, Figure 5, Figure 6). Although it is still debated whether
376 NS primarily function as storage sites or as active hubs for RNA metabolism, our findings
377 support the latter view by linking speckle organization to both defined molecular interactions
378 and functional splicing outcomes. It should also be noted that STA1 itself appeared to form
379 non-functional aggregates under heat conditions due to its IDRs (Supplemental Figure 6).
380 DOT2 seemed to inhibit the aggregation of STA1 and direct STA1 to NS, presumably

381 facilitating formation of an active spliceosome. Thus, STA1-DOT2 interaction contributes to
382 the robustness of pre-mRNA splicing under heat stress.

383 Taken together, our study expands current understanding of NS biology by
384 demonstrating that NS organization in plants is closely associated with the assembly state of
385 the spliceosome, mediated by specific protein–protein interactions within the U4/U6·U5 tri-
386 snRNP. On this basis, we propose that heat-sensitive interaction nodes such as the STA1-DOT2
387 bridge represent "molecular weak points" or "interaction-level sensors" that integrate
388 spliceosome architecture, subnuclear organelle formation, and environmental responsiveness.
389 This interaction-based perspective provides insight into how plants maintain splicing
390 robustness under stress conditions and suggests that targeted modulation of spliceosomal
391 interactions may offer a potential strategy for improving stress tolerance.

392 **METHODS**

393 **Plant growth conditions**

394 *Arabidopsis thaliana* seeds were planted on Murashige and Skoog (MS) medium
395 containing MS salts with vitamins (Caisson Laboratories Inc, USA), 2% sucrose, and 0.3%
396 gelite (Duchefa, the Netherlands), adjusted to pH 5.7-5.8. For vertical growth, 0.6% gelrite was
397 supplemented. Seeds were surface-sterilized with commercial bleach supplemented with 0.01%
398 Tween 20 (USB, USA), stratified at 4°C for 2 days in the dark, and then transferred to a growth
399 chamber under long-day conditions (16 h light/8 h dark) at 22°C. For soil-grown plants, seeds
400 were sown on Sun Gro propagation mix (Sun Gro, Canada) and maintained under long-day
401 conditions (16 h light/8 h dark) at 22°C.

402 **Positional cloning and mutation identification**

403 To map the *S307* mutation locus, *S307* (Columbia background) was crossed with
404 Landsberg *erecta* (L*er*) to generate an F2 mapping population. WT-sized F2 plants homozygous
405 for the *sta1-1* mutation were selected, and recovery of the size phenotype was confirmed in the
406 F3 population pool. Genomic DNA was extracted from pooled leaves of 94 selected F2 mutant
407 individuals using the RNeasy Plant Mini Kit (QIAGEN, Germany), and whole-genome
408 sequencing was performed at Macrogen Inc. The genomic region between the SSLP markers
409 Ch5_5.46 Mb and Ch5_5.71Mb, identified by initial mapping, was compared with the WT
410 genomic sequence, identifying a candidate point mutation at position 1,651 bp of *DOT2*
411 (At5g16780) coding sequence. The candidate mutation was validated by complementation
412 using genomic constructs driven by either the native *DOT2* promoter (DOT2::DOT2) or the
413 Cauliflower mosaic virus 35S promoter (35S::DOT2). For native *DOT2* promoter
414 complementation lines ($S307^{DOT2END}$), a 3,783 bp genomic fragment spanning 1,695 bp
415 upstream of the DOT2 start codon to 294 bp downstream of the stop codon was amplified and
416 cloned into pCAMBIA1300 between the *Kpn*I and *Bam*HI sites (Takara, Japan). For 35S-
417 driven complementation lines ($S307^{DOT2OX}$), the 2,463 bp *DOT2* coding sequence was
418 amplified, cloned into pDONR221 entry vector, and subsequently recombined into the
419 pMDC32 destination vector using the Gateway cloning system. All primers used to generate
420 complementation constructs are listed in Supplemental Table S1.

421 **Generation of different alleles of *dot2* mutants**

422 The *dot2* single mutant carrying the *S307* allele (*dot2*^{S}) was obtained from the F2
423 progeny of a cross between WT and *S307*. A derived cleaved amplified polymorphic sequence
424 (dCAPS) marker detecting the single-nucleotide substitution in the *dot2*^{S} allele using *Eco*RI
425 (Takara, Japan), together with a marker detecting the 6-nucleotide deletion in *sta1-1* (used to
426 exclude plants carrying the *sta1-1* mutation), was employed to isolate the *dot2*^{S} single mutant.
427 The *dot2* T-DNA insertion mutant *SAIL_775_F10* (*dot2*^{T}) was obtained from the Arabidopsis
428 Biological Resource Center (ABRC). Because homozygous *dot2*^{T} plants are infertile, only
429 heterozygotes were maintained, and homozygotes were identified by their dwarf phenotype
430 (Petricka et al., 2008).

431 A CRISPR/Cas9-generated *dot2* mutant allele (*dot2*^{C}) was produced in the *sta1-1*
432 background using the CRISPR/Cas9 system as previously described (Cho et al., 2017; Liu et
433 al., 2015; Yun et al., 2022). A single guide RNA (sgRNA) targeting *DOT2* was designed using
434 the CRISPR web toolbox CHOPCHOP (https://chopchop.cbu.uib.no) (Labun et al., 2019). The
435 annealed oligonucleotides (DOT2sgRNA3_infu_CF and DOT2sgRNA3_infu_CR) for sgRNA
436 were cloned into the psgR-Cas9-At to generate *DOT2*-targeting construct. The resultant
437 DOT2sgRNA3-Cas9 cassette, excised with *Hin*dIII and *Eco*RI (Takara, Japan), was
438 subsequently subcloned into the *Hin*dIII-*Eco*RI sites of pCAMBIA1300. *Agrobacterium*
439 *tumefaciens* strain GV3101 carrying these constructs was used to transform *sta1-1* plants by
440 the floral dip method to obtain T1 seeds. CRISPR/Cas9-edited elite lines were identified by
441 Sanger sequencing of the DOT2sgRNA3-targeted region in the T1 generation, and
442 homozygous lines were subsequently isolated. All primers used for the isolation of different
443 *dot2* mutant allels are listed in Supplemental Table S1.

444 **RNA extraction and cDNA synthesis**

445 Total RNA was extracted from seedlings at the designated developmental stage using
446 RNAiso Plus reagent (Takara, Japan) and treated with RNase-free DNase (New England
447 BioLabs, USA). cDNA was synthesized from total RNA using the TOPscript^{TM} Reverse
448 Transcriptase kit (Enzynomics, Korea). Semi-quantitative RT-PCR and realtime PCR analyses
449 were performed using 2 μL of the resulting cDNA (corresponding to 50 ng of input RNA). All

450 primers used for intron retention analyses and gene expression quantification are listed in
451 Supplemental Table S1.

452 **GUS staining assay**

453 For the *STA1* promoter-driven *GUS* (*STA1::GUS*) and *DOT2* promoter-driven *GUS*
454 (*DOT2::GUS*) constructs, 1,475 bp and 1,695 bp promoter fragments upstream of the start
455 codon of each gene were amplified, respectively. These fragments were cloned into
456 pCAMBIA1381 between the *Bam*HI and *Hind*III sites for *STA1::GUS*, or between the *Bam*HI
457 and *Nco*I sites for *DOT2::GUS* (Takara, Japan). *Agrobacterium tumefaciens* strain GV3101
458 carrying these constructs was used to transform Col-0 plants by the floral dip method.

459 Tissues of transgenic *Arabidopsis* seedlings carrying the *STA1::GUS* or *DOT2::GUS*
460 constructs were collected in 90% acetone (Duksan, Korea) in conical tubes on ice and incubated
461 for 10-20 min at room temperature. After removal of acetone, samples were washed twice for
462 5 min with washing buffer (50 mM potassium phosphate buffer (pH = 7.0), 0.2% Triton X-100,
463 2 mM potassium ferricyanide, and 2 mM potassium ferrocyanide). The washing buffer was
464 then replaced with staining buffer (washing buffer supplemented with 2 mM X-Gluc (Sigma,
465 Japan), and tissues were incubated overnight at 37°C. Subsequently, tissues were incubated in
466 70% ethanol to remove chlorophyll. GUS-staining was observed using a light microscope
467 (Leica ICC50, Germany).

468 **Nuclear localization, co-localization, and BiFC analyses**

469 For nuclear localization analyses, the full-length coding regions of *STA1* (*sta1-1*)
470 lacking a stop codon and *DOT2* (*dot2*^{S} and *dot2*^{C}) containing a stop codon were amplified,
471 cloned into pDONR221 entry vector, and subsequently recombined into the pGWB551 or
472 pGWB552 destination vectors, respectively, using the Gateway cloning system. *Agrobacterium*
473 *tumefaciens* cells harboring STA1 (sta1-1)-GFP or GFP-DOT2 (dot2^{S} and dot2^{C}) constructs
474 were infiltrated into *Nicotiana benthamiana* leaves in expression buffer (50 mM MES (pH =
475 5.7), 10 mM $MgSO_4$, 5% D-Glucose, and 0.1 mM of acetosyringone) together with P19, each
476 at a final concentration of OD_{600} of 0.2. After 36 h of incubation of infiltrated *N. benthamiana*
477 at 22°C, fluorescence images were acquired using a confocal microscope (TCS SP5 or
478 STELLARIS; Leica, Germany). GFP signals were excited at 488 nm and detected at 500-530

479 nm. For heat treatment, samples were incubated in liquid MS medium (0.5x MS mineral salts,
480 1% sucrose, 5 mM 2-(N-Morpholino) ethanesulfonic acid (MES; Sigma, Japan), pH adjusted
481 to 5.7 with KOH) for 1 h at 37°C following the initial 36 h incubation.

482 For co-localization analyses, the full-length DOT2 (dot2^{S} and dot2^{C}) coding region
483 containing a stop codon was cloned downstream of the CaMV 35S promoter and fused in frame
484 with mRFP in the p35S-FAST-mRFP vector. *Agrobacterium* cultures carrying STA1 (sta1-1)-
485 GFP and mRFP-DOT2 (dot2^{S} and dot2^{C}) constructs were co-infiltrated into *N. benthamiana*
486 leaves and fluorescent signals were observed as described above. RFP signals were excited at
487 532 nm and detected at 580-620 nm.

488 For BiFC analyses, the same entry clones used for nuclear localization analyses were
489 used. STA1 (sta1-1) and DOT2 (dot2^{S} and dot2^{C}) entry clones were recombined downstream
490 of the CaMV 35S promoter and fused in frame with nEYFP or cEYFP in the pSITE-nEYFP-
491 N1 (GU734648) or pSITE-cEYFP-C1 (GU734652) Gateway vectors, respectively.
492 *Agrobacterium* cells carrying pSITE-STA1 (sta1-1)-nEYFP or pSITE-cEYFP-DOT2 (dot2^{S}
493 and dot2^{C}) constructs were co-infiltrated in combination into *N. benthamiana* leaves in the
494 indicated combinations, and fluorescent signals were observed as described above. EYFP
495 signals were excited at 488 nm and detected at 500-530 nm. As a nuclear speckle marker, the
496 full-length coding region of *U1-70K* (*At3g50670*) was amplified and cloned into p35S-FAST-
497 mRFP between the *Bam*HI and *Sal*I (Enzynomics, Korea) sites. As a nucleolus marker,
498 FIBRILLARIN 2 (FIB2, At4g25630)-mRFP, provided by Dr. Hyun-Sook Pai, was used (Park
499 et al., 2021). All primers used to generate constructs are listed in Supplemental Table S1.

500 **Yeast two-hybrid assay**

501 The full-length coding region of *STA1* or *sta1-1* was inserted into the pGADT7 vector,
502 and *DOT2* or *dot2^{S}* was inserted into the pGBKT7 vector. The resulting constructs, pGADT7-
503 STA1 (sta1-1) as prey and pGBKT7-DOT2 (dot2^{S}) as bait, were co-transformed into the
504 *Saccharomyces cerevisiae* strain AH109 (Takara, Japan) and incubated at 30°C for 3 days.
505 Transformants were selected on SD/-Leu/-Trp or SD/-Leu/-Trp/-His medium supplemented
506 with 3-amino-1,2,4-triazole (3-AT; Sigma, Japan), a competitive inhibitor of the *HIS3* gene
507 product. All primers used to generate constructs are listed in Supplemental Table S1.

508 **Arabidopsis mesophyll protoplast transient expression assay**

509 Protoplast isolation and transient expression assays were performed as previously
510 described (Kim *et al.*, 2017). Effector constructs (STA1, sta1-1, DOT2, dot2^{S}, and dot2^{C}) and
511 reporter constructs (g*HSFA3* fused to NanoLuc luciferase (nLUC) were generated by inserting
512 the corresponding coding sequences between the HBT promoter (a modified CaMV 35S
513 promoter) and the NOS terminator in a plant expression vector. Firefly luciferase (fLUC),
514 driven by the *UBQ10* promoter, was included as an internal control.

515 For nuclear localization analysis in protoplasts, HBT-DOT2 (dot2^{S} and dot2^{C})
516 constructs were transfected to *Salk007933*$^{STA1\text{-}GFP}$ or *Salk007933*$^{sta1\text{-}1\text{-}GFP}$. Fluorescence images
517 were acquired using a confocal microscope (TCS SP5; Leica, Germany). GFP signals were
518 excited at 488 nm and detected at 500-530 nm.

519 For functional splicing assays, HBT-DOT2 (dot2^{S} and dot2^{C}) constructs were
520 transfected to *Salk007933*$^{sta1\text{-}1\text{-}GFP}$ and reporter activities were calculated as the nLUC/fLUC
521 ratio. Transfected protoplasts were lysed in passive lysis buffer (Promega, USA) containing 1%
522 Triton X-100 (USB, USA) and briefly vortexed. Lysates were incubated at room temperature
523 for 10 minutes and then centrifuged at 13,000 rpm for 30 s. The supernatant was transferred
524 for measurement of fLUC and nLUC activities using the Nano-Glo® Dual-Luciferase®
525 Reporter Assay System (Promega, USA) and a GloMax 20/20 Luminometer (Promega, USA).
526 All primers used to generate constructs are listed in Supplemental Table S1.

527 **Pollen viability**

528 To assess pollen viability, 2-month-old plants were subjected to heat treatment (37°C
529 for 1 day) or maintained under control conditions. Pollen grains were stained using the
530 Alexander staining method as previously described (Peterson, 2010). Flower buds prior to
531 anthesis were collected and fixed in Carnoy's fixative (6 ethanol : 3 chloroform : 1 acetic acid)
532 for at least 2 h. Fixed flower buds were then stained in the final staining solution at 50°C for 2
533 min. Stained pollen grains were observed using a light microscope (Leica ICC50, Germany).

534 **Propidium iodide staining**

535 Seedlings from 3-day-old plants were collected and incubated in a 10 μg/mL

propidium iodide (PI) solution (Sigma, Japan) for 1 min. Seedlings were then washed with distilled water and observed using a Leica TCS SP5 laser scanning confocal microscope (Leica, Germany). PI fluorescence was excited at 532 nm and detected at 590–630 nm.

RNA-seq analysis

Total RNA was extracted from 7-day-old WT, *sta1-1*, and *S307* seedlings using RNAiso Plus (Takara, Japan). Heat stress (37°C for 3 h) was applied to 7-day-old plants, and heat-treated samples were collected. Three independent biological replicates were prepared for each condition. Sequencing libraries were constructed using the TruSeq Stranded mRNA Library Prep Kit with indexed adapters and RNA sequencing was performed using the Illumina NovaSeq platform (MacroGen, Korea). Paired-end raw sequencing reads were pre-processed to trim adaptors and low-quality reads using CLC Genomics Workbench v20.0.4 with default parameters (quality scores, 0.05; maximum ambiguous nucleotides, 2). Clean reads were mapped to *Arabidopsis* reference genome (TAIR10). Intron retention ratios at the whole-transcript level were estimated using IRFinder (v.1.3.0) (Middleton et al., 2017). Intron retention events were defined as those showing a change in IR ratio (ΔIR ratio) greater than 0.1 with an adjusted *p*-value (p_{adj}) < 0.05. IR ratios were transformed into z-scores and visualized as heatmaps. Volcano plots were used to assess the overall distribution of IR changes in each comparison. RNA sequencing data have been deposited in the Gene Expression Omnibus (GEO) under accession number XXX.

FUNDING

This work was supported by the National Research Foundation of Korea grant funded by the Korean government (MSIT) (RS-2024-00355816 to D.-H.J., RS-2024-00407469 for D.J.Y. and B.-h.L. and RS-2025-00564152 for B.-h.L.) and G-LAMP grant (NRF) funded by the Korean government (MOE) (RS-2024-00441954 for B.-h.L.), Korea Basic Science Institute (National Research Facilities and Equipment Center) grant funded by the Korean government (MOE) (RS-2020-NF000322 for B.-h.L.), and the Basic Science Research Program (NRF) funded by the Korean government MOE (2018R1A6A1A03025607 for W.T.K.).

ACKNOWLEDGMENTS

We would like to thank our lab members, as well as Inki Kim (Asan Medical Center, Korea), Dr. Hyun-Sook Pai (Yonsei University, Korea) and Dr. Jae-Hoon Jung (Sungkyunkwan University, Korea), for technical assistance, materials and helpful discussion. The authors declare no conflict of interest.

AUTHOR CONTRIBUTIONS

H.K., K.-j.Y., S.P., and D.S. conducted the experiments and performed bioinformatic analyses. W.T.K., D.-H.J., D.J.Y., and B.-h.L. advised on the research. All authors discussed the results. H.K. and B.-h.L. wrote the manuscript.

575 **REFERENCES**

576 **Bertram, K., Agafonov, D.E., Dybkov, O., Haselbach, D., Leelaram, M.N., Will, C.L., Urlaub, H.,**
577 **Kastner, B., Lührmann, R., and Stark, H.** (2017). Cryo-EM Structure of a Pre-catalytic Human
578 Spliceosome Primed for Activation. Cell. **170**:701-713.

579 **Bhat, P., Chow, A., Emert, B., Ettlin, O., Quinodoz, S.A., Strehle, M., Takei, Y., Burr, A., Goronzy,**
580 **I.N., Chen, A.W., et al.** (2024). Genome organization around nuclear speckles drives mRNA
581 splicing efficiency. Nature. **629**

582 **Bond, U.** (1988). Heat shock but not other stress inducers leads to the disruption of a sub-set of snRNPs
583 and inhibition of in vitro splicing in HeLa cells. EMBO J. **7**:3509-3518.

584 **Bond, U., and James, T.C.** (2000). Dynamic changes in small nuclear ribonucleoproteins of heat-
585 stressed and thermotolerant HeLa cells. Int J Biochem Cell Biol. **32**:643-656.

586 **Cho, S., Yu, S.I., Park, J., Mao, Y.F., Zhu, J.K., Yun, D.J., and Lee, B.H.** (2017). Accession-
587 Dependent CBF Gene Deletion by CRISPR/Cas System in Arabidopsis. Front. Plant Sci. **8**

588 **Choi, S., Ha, S., Wolfgeher, D.J., Kim, J.W., Go, Y.H., Cha, H.J., Bae, G.U., Kron, S.J., and Kim,**
589 **W.Y.** (2025). N-Terminal deleted isoforms of E3 ligase RNF220 are ubiquitously expressed and
590 required for mouse muscle differentiation. Mol. Cell. **48**

591 **Daguenet, E., Baguet, A., Degot, S., Schmidt, U., Alpy, F., Wendling, C., Spiegelhalter, C., Kessler,**
592 **P., Rio, M.C., Le Hir, H., et al.** (2012). Perispeckles are major assembly sites for the exon
593 junction core complex. Mol Biol Cell. **23**:1765-1782.

594 **Day, I.S., Golovkin, M., Palusa, S.G., Link, A., Ali, G.S., Thomas, J., Richardson, D.N., and Reddy,**
595 **A.S.N.** (2012). Interactions of SR45, an SR-like protein, with spliceosomal proteins and an
596 intronic sequence: insights into regulated splicing. Plant J. **71**:936-947.

597 **de Luxan-Hernandez, C., Lohmann, J., Tranque, E., Chumova, J., Binarova, P., Salinas, J., and**
598 **Weingartner, M.** (2022). MDF is a conserved splicing factor and modulates cell division and
599 stress response in Arabidopsis. Life Sci. Alliance. **6**

600 **Galisson, F., and Legrain, P.** (1993). THE BIOCHEMICAL DEFECTS OF PRP4-1 AND PRP6-1
601 YEAST SPLICING MUTANTS REVEAL THAT THE PRP6 PROTEIN IS REQUIRED FOR
602 THE ACCUMULATION OF THE [U4/U6.U5] TRI-SNRNP. Nucl Acids Res. **21**:1555-1562.

603 **Häcker, I., Sander, B., Golas, M.M., Wolf, E., Karagoez, E., Kastner, B., Stark, H., Fabrizio, P.,**
604 **and Lührmann, R.** (2008). Localization of Prp8, Brr2, Snu114 and U4/U6 proteins in the yeast
605 tri-snRNP by electron microscopy. Nat. Struct. Mol. Biol. **15**:1206-1212.

606 **Ilik, I.A., Malszycki, M., Lübke, A.K., Schade, C., Meierhofer, D., and Aktas, T.** (2020). SON and
607 SRRM2 are essential for nuclear speckle formation. eLife. **9**

608 **Kim, C.H., Kim, Y.D., Choi, E.K., Kim, H.R., Na, B.R., Im, S.H., and Jun, C.D.** (2016). Nuclear
609 Speckle-related Protein 70 Binds to Serine/Arginine-rich Splicing Factors 1 and 2 via an
610 Arginine/Serine-like Region and Counteracts Their Alternative Splicing Activity. J. Biol. Chem.
611 **291**:6169-6181.

Kim, G.D., Yoo, S.D., and Cho, Y.H. (2018). STABILIZED1 as a heat stress-specific splicing factor in Arabidopsis thaliana. Plant Signal Behav. **13**

Kim, G.D., Cho, Y.H., Lee, B.H., and Yoo, S.D. (2017). STABILIZED1 Modulates Pre-mRNA Splicing for Thermotolerance. Plant Physiol. **173**:2370-2382.

Klimesová, K., Vojácková, J., Radivojevic, N., Vandermoere, F., Bertrand, E., Verheggen, C., and Stanek, D. (2021). TSSC4 is a component of U5 snRNP that promotes tri-snRNP formation. Nat. Commun. **12**

Krissinel, E., and Henrick, K. (2007). Inference of macromolecular assemblies from crystalline state. J. Mol. Biol. **372**:774-797.

Ku, D., Yang, Y., and Kim, Y. (2025). RNA-associated nuclear condensates: Where the nucleus keeps its RNAs in check. Mol. Cells. **48**

Kurogi, Y., Matsuo, Y., Mihara, Y., Yagi, H., Shigaki-Miyamoto, K., Toyota, S., Azuma, Y., Igarashi, M., and Tani, T. (2014). Identification of a chemical inhibitor for nuclear speckle formation: Implications for the function of nuclear speckles in regulation of alternative pre-mRNA splicing. Biochem. Biophys. Res. Commun. **446**:119-124.

Labun, K., Montague, T.G., Krause, M., Cleuren, Y.N.T., Tjeldnes, H., and Valen, E. (2019). CHOPCHOP v3: expanding the CRISPR web toolbox beyond genome editing. Nucl Acids Res. **47**:W171-W174.

Lee, B.H., Kapoor, A., Zhu, J.H., and Zhu, J.K. (2006). STABILIZED1, a stress-upregulated nuclear protein, is required for pre-mRNA splicing, mRNA turnover, and stress tolerance in Arabidopsis. Plant Cell. **18**:1736-1749.

Li, J., Cao, Y.M., Zhang, J.X., Zhu, C.J., Tang, G.L., and Yan, J. (2023). The miR165/166-PHABULOSA module promotes thermotolerance by transcriptionally and posttranslationally regulating HSFA1. Plant Cell. **35**:2952-2971.

Liang, Q.Y., Peng, N.N., Xie, Y., Kumar, N., Gao, W.B., and Miao, Y.S. (2024). MolPhase, an advanced prediction algorithm for protein phase separation. EMBO J. **43**:1898-1918.

Liu, S.B., Rauhut, R., Vornlocher, H.P., and Lührmann, R. (2006). The network of protein-protein interactions within the human U4/U6.U5 tri-snRNP. RNA. **12**:1418-1430.

Liu, S.Y., Wang, T.S., Shi, Y.L., Bai, L., Wang, S.S., Guo, D., Zhang, Y., Qi, Y.F., Chen, C.Q., Zhang, J.R., et al. (2021). USP42 drives nuclear speckle mRNA splicing via directing dynamic phase separation to promote tumorigenesis. Cell Death Differ. **28**:2482-2498.

Liu, W.S., Zhu, X.H., Lei, M.G., Xia, Q.Y., Botella, J.R., Zhu, J.K., and Mao, Y.F. (2015). A detailed procedure for CRISPR/Cas9-mediated gene editing in Arabidopsis thaliana. Sci. Bull. **60**:1332-1347.

Ma, J., Li, S., Wang, T.Y., Tao, Z., Huang, S.J., Lin, N., Zhao, Y.B., Wang, C.H., and Li, P.J. (2025). Cooperative condensation of RNA-DIRECTED DNA METHYLATION 16 splicing isoforms enhances heat tolerance in Arabidopsis. Nat Commun. **16**

Makarov, E.M., Makarova, O.V., Achsel, T., and Lührmann, R. (2000). The human homologue of the yeast splicing factor Prp6p contains multiple TPR elements and is stably associated with the U5 snRNP via protein-protein interactions. J. Mol. Biol. **298**:567-575.

Makarova, O.V., Makarov, E.M., and Lührmann, R. (2001). The 65 and 110 kDa SR-related proteins of the U4/U6•U5 tri-snRNP are essential for the assembly of mature spliceosomes. EMBO J. **20**:2553-2563.

Middleton, R., Gao, D.D., Thomas, A., Singh, B., Au, A., Wong, J.J.L., Bomane, A., Cosson, B., Eyras, E., Rasko, J.E.J., et al. (2017). IRFinder: assessing the impact of intron retention on mammalian gene expression. Genome Biol. **18**

Mintz, P.J., Patterson, S.D., Neuwald, A.F., Spahr, C.S., and Spector, D.L. (1999). Purification and biochemical characterization of interchromatin granule clusters. EMBO J. **18**:4308-4320.

Negi, S.S., Schein, C.H., Oezguen, N., Power, T.D., and Braun, W. (2007). InterProSurf: a web server for predicting interacting sites on protein surfaces. Bioinform. **23**:3397-3399.

Nguyen, T.H.D., Galej, W.P., Bai, X.C., Oubridge, C., Newman, A.J., Scheres, S.H.W., and Nagai, K. (2016). Cryo-EM structure of the yeast U4/U6.U5 tri-snRNP at 3.7 Å resolution. Nature. **530**:298-302.

Nishizawa-Yokoi, A., Nosaka, R., Hayashi, H., Tainaka, H., Maruta, T., Tamoi, M., Ikeda, M., Ohme-Takagi, M., Yoshimura, K., Yabuta, Y., et al. (2011). HsfA1d and HsfA1e Involved in the Transcriptional Regulation of HsfA2 Function as Key Regulators for the Hsf Signaling Network in Response to Environmental Stress. Plant Cell Physiol. **52**:933-945.

Park, S.J., Choi, S.W., Kim, G.M., Moller, C., Pai, H.S., and Yang, S.W. (2021). Light-stabilized FHA2 suppresses miRNA biogenesis through interactions with DCL1 and HYL1. Mol. Plant. **14**:647-663.

Park, S.Y., Chang, H.S., Lim, S.H., Jeong, D.H., and Kim, Y.J. (2024). Functional Characterization of PRP43a, a Component for Splicing Disassembly in Arabidopsis. J. Plant Biol. **67**:427-435.

Paul, S., Arias, M.A., Wen, L., Liao, S.E., Zhang, J.C., Wang, X.S., Regev, O., and Fei, J.Y. (2024). RNA molecules display distinctive organization at nuclear speckles. iScience. **27**

Peterson, R.S., J. P. Chen, C. (2010). A simplified method for differential staining of aborted and non-aborted pollen grains. Int. J. Plant Biol. **1**:e13-e13.

Petricka, J.J., Clay, N.K., and Nelson, T.M. (2008). Vein patterning screens and the defectively organized tributaries mutants in Arabidopsis thaliana. Plant J. **56**:251-263.

Röth, S., Mirus, O., Bublak, D., Scharf, K.D., and Schleiff, E. (2017). DNA-binding and repressor function are prerequisites for the turnover of the tomato heat stress transcription factor HsfB1. Plant J. **89**:31-44.

Sander, B., Golas, M.M., Makarov, E.M., Brahms, H., Kastner, B., Luehrmann, R., and Stark, H. (2006). Organization of core spliceosomal components U5 snRNA loop I and U4/U6 Di-snRNP within U4/U6.U5 tri-snRNP as revealed by electron cryomicroscopy. Mol Cell. **24**:267-278.

Schaffert, N., Hossbach, M., Heintzmann, R., Achsel, T., and Lührmann, R. (2004). RNAi knockdown of hPrp31 leads to an accumulation of U4/U6 di-snRNPs in Cajal bodies. EMBO J. **23**:3000-3009.

Schneider, M., Hsiao, H.H., Will, C.L., Giet, R., Urlaub, H., and Lührmann, R. (2010). Human PRP4 kinase is required for stable tri-snRNP association during spliceosomal B complex formation. Nat. Struct. Mol. Biol. **17**:216-U212.

Smith, K.P., Hall, L.L., and Lawrence, J.B. (2020). Nuclear hubs built on RNAs and clustered organization of the genome. Curr. Opin. Cell Biol. **64**:67-76.

Sun, M.L., Zhang, Y.M., Wang, Q.H., Wu, C.L., Jiang, C., and Xu, J.R. (2018). The tri-snRNP specific protein FgSnu66 is functionally related to FgPrp4 kinase in Fusarium graminearum. Mol. Microbiol. **109**:494-508.

Utans, U., Behrens, S.E., Luhrmann, R., Kole, R., and Kramer, A. (1992). A SPLICING FACTOR THAT IS INACTIVATED DURING INVIVO HEAT-SHOCK IS FUNCTIONALLY EQUIVALENT TO THE [U4/U6.U5] TRIPLE SNRNP-SPECIFIC PROTEINS. Genes Dev. **6**:631-641.

Wang, B., Li, J., Song, Y.Y., Qin, X.H., Lu, X., Huang, W., Peng, C.T., Wei, J.X., Huang, D.H., and Wang, W. (2024). CLK2 Condensates Reorganize Nuclear Speckles and Induce Intron Retention. Adv. Sci. **11**

Will, C.L., and Lührmann, R. (2011). Spliceosome Structure and Function. CSH Perspect. Biol. **3**

Wu, J.J., Xiao, Y., Liu, Y.Z., Wen, L., Jin, C.Y., Liu, S., Paul, S., He, C., Regev, O., and Fei, J.Y. (2024). Dynamics of RNA localization to nuclear speckles are connected to splicing efficiency. Sci. Adv. **10**

Yildirim, A., Mozaffari-Jovin, S., Wallisch, A.K., Schaefer, J., Ludwig, S.E.J., Urlaub, H., Luehrmann, R., and Wolfrum, U. (2021). SANS (USH1G) regulates pre-mRNA splicing by mediating the intra-nuclear transfer of tri-snRNP complexes. Nucl Acids Res. **49**:5845-5866.

Yun, J.Y., Yu, S.I., Bang, S.E., Kim, J.Y., Lee, S.H., and Lee, B.H. (2022). Identification of CRISPR-Induced Mutations in Plants: with a Focus on the Next-Generation Sequencing Assay. J. Plant Biol. **65**:435-443.

Zeytuni, N., and Zarivach, R. (2012). Structural and Functional Discussion of the Tetra-Trico-Peptide Repeat, a Protein Interaction Module. Structure. **20**:397-405.

Zhan, X.C., Yan, C.Y., Zhang, X.F., Lei, J.L., and Shi, Y.G. (2018). Structures of the human pre-catalytic spliceosome and its precursor spliceosome. Cell Res. **28**:1129-1140.

Zhang, M.J., Gu, Z., Guo, S.H., Sun, Y.T., Ma, S.B., Yang, S., Guo, J.R., Fang, C.X., Shu, L., Ge, Y.F., et al. (2024). SRRM2 phase separation drives assembly of nuclear speckle subcompartments. Cell Rep. **43**

723 **Figure Legends**

724

725 **Figure 1. The *dot2^S* mutation in *S307* rescues *sta1-1* defects and restores interaction with**
726 **the sta1-1 protein**

727 **(A)** Growth phenotypes and fresh weights of 3-week-old WT, *sta1-1*, and *S307* plants (scale
728 bar = 5 cm; n = 22).

729 **(B)** Heatmap showing IR ratios in WT, *sta1-1*, and *S307*. Three independent biological
730 replicates were analyzed for each genotype.

731 **(C)** Volcano plots showing significantly repressed and induced IR events. Blue and red dots
732 represent significantly decreased and increased IR events, respectively.

733 **(D)** Growth phenotypes of 3-week-old WT, *sta1-1*, *S307*, *S307^{DOT2END}*, and *S307^{DOT2OX}* plants
734 (scale bar = 5 cm).

735 **(E)** Experimental validation of IR levels for representative genes (*Leaf curly and small 1* (*FCS1*,
736 At1g78910), *BOI-RELATED GENE 1* (*BRG1*, At5g45100), and *BETA GLUCOSIDASE 6*
737 (*BGLU6*, At1g60270). Box diagrams show spliced and unspliced isoforms. *Protein*
738 *phosphatase 2A* (*PP2A*, At1g13320) is used as a loading control.

739 **(F and G)** Semi-dominant effects of the *dot2^S* mutation on plant growth and splicing in the
740 *sta1-1* mutant background (scale bar = 1 cm). Three-week-old plants derived from an F2
741 population segregating for both the *sta1-1* and *dot2^S* alleles (WT x *S307* cross). Genotypes are
742 indicated as follows; *S*, *STA1*; *s, sta1-1*; *D, DOT2*; *d^S*, *dot2^S*. *PP2A* is used as a loading control.
743 Box diagrams showed spliced and unspliced isoforms.

744 **(H)** Y2H assays demonstrating the interaction between STA1/sta1-1 and DOT2/dot2^S. Yeast
745 cells co-transformed with the fusion constructs of the GAL4 DNA-binding domain and
746 activation domain were grown overnight and spotted onto selection medium (-L/-W), and
747 interaction medium (-L/-W/-H) supplemented with 0.5 mM 3-amino-1,2,4-triazole (3-AT).

748 **(I and J)** BiFC analysis for detecting the interaction between STA1/sta1-1 and
749 DOT2/dot2^S/dot2^C in leaves of *N. benthamiana* (scale bar = 75 μm). Red arrows indicate EYFP
750 signals representing protein-protein interactions in the nucleus. EYFP signals were quantified
751 from identical areas of leaf disks (2 x 2 cm). Data are presented as mean ± SE (n = 5).
752 Statistical analysis is performed using one-way ANOVA with Tukey's HSD test (**$P < 0.01$;
753 n.s., not significant).

754

755 **Figure 2. The disrupted nuclear localization of sta1-1 protein is re-localized to NS by the**
756 **dot2^{S} protein**

757 **(A)** Classification of nuclear compartments showing the localization of gene of interest (GOI)-
758 GFP driven by the CaMV 35S promoter into five subclasses. The nucleolus marker
759 FIBRILLARIN 2 (FIB2, At4g25630)-mRFP was co-infiltrated (scale bar = 10 μm).

760 **(B)** Subcellular localization of each protein tagged with GFP in leaves of *N. benthamiana*.
761 Nuclear localization patterns of each GFP-tagged protein were classified into the five distinct
762 categories defined in **(A)**. For each set, 100 GFP-expressing cells were analyzed per replicate,
763 and data are presented as mean ± SE (n = 4). Statistical analysis is performed using one-way
764 ANOVA with Tukey's HSD test (**$P < 0.01$; n.s., not significant).

765 **(C-E)** Co-localization of GFP-tagged STA1/sta1-1 with mRFP-tagged DOT2/dot2^{S}/dot2^{C} in
766 leaves of *N. benthamiana*. Nuclear localization categories are shown in **(D)**, classified
767 according to the groups defined in **(A)**. The number of NS per nucleus is shown in **(E)**, based
768 on the STA1/sta1-1-GFP signals upon co-expression with mRFP-DOT2/dot2^{S}/dot2^{C}. For each
769 analysis, 100 cells **(D)** or 50 nuclei **(E)** were randomly selected and analyzed (scale bar = 10
770 μm).

771 **(F-H)** Co-localization of GFP-tagged STA1 **(F and H)** or EYFP signals from BiFC analysis of
772 STA1 and DOT2 **(G)** with the NS marker U1 SMALL NUCLEAR RIBONUCLEOPROTEIN-
773 70K (U1-70K, At3g50670) tagged with mRFP (mRFP-U1-70K) in leaves of *N. benthamiana*.
774 Red boxes indicate regions of overlap between STA1-GFP and mRFP-U1-70K (scale bar = 10
775 μm).

776

777 **Figure 3. The localization of STA1 to NS is closely associated with proper pre-mRNA**
778 **splicing**

779 **(A)** Nuclear localization patterns of GFP-tagged STA1/sta1-1 upon transfection with
780 DOT2/dot2^{S}/dot2^{C} in *Salk007933$^{STA1\text{-}GFP}$* or *Salk007933$^{sta1\text{-}1\text{-}GFP}$* protoplasts. Cells with
781 nuclear-localized GFP signals of two distinct patterns (nucleoplasm and NS) were quantified
782 as a ratio. A total of 15 cells were analyzed for each combination (scale bar = 5 μm).

783 **(B)** Splicing activity of DOT2/dot2^{S}/dot2^{C} on the *gHSFA3* DNA in *Salk007933*$^{sta1\text{-}1\text{-}GFP}$
784 protoplasts. Splicing activity on the *gHSFA3* DNA is represented by the relative expression of
785 NanoLuc luciferase (nLUC) compared with firefly luciferase (fLUC). *Clathrin* (At4g24550)
786 was used as a loading control. Data are presented as mean ± SE (n = 2). Statistical analysis is
787 performed using one-way ANOVA with Tukey's HSD test ($^{**}P < 0.01$; n.s., not significant).
788 **(C)** Tubercidin-induced delocalization of STA1 from NS to nucleoplasm. Ten-day-old
789 *Salk007933*$^{STA1\text{-}GFP}$ plants were treated with DMSO or 100 μM tubercidin for 1 h (scale bar =
790 25 μm).
791 **(D)** Tubercidin-induced disruption of pre-mRNA splicing. Ten-day-old WT, *sta1-1*, and *S307*
792 plants were treated with DMSO or 100 μM tubercidin for 12 h. The box diagrams show spliced
793 and unspliced isoforms. *PP2A* is used as a loading control.
794 **(E)** Abolished size differences between WT, *sta1-1*, and *S307* by tubercidin treatment (scale
795 bar = 1 cm). Five-day-old seedlings were transferred to medium containing either DMSO or
796 10 μM tubercidin for 6 d. Data are presented as mean ± SE (n = 4).
797
798 **Figure 4. The dot2^{S} protein facilitates NS localization of the sta1-1 protein under heat**
799 **conditions**
800 **(A-C)** BiFC analysis to detect interaction between STA1 and DOT2 under heat stress
801 conditions in leaves of *N. benthamiana* (scale bar = 75 μm). Red arrows indicate EYFP signals
802 representing protein-protein interactions in the nucleus. The number of EYFP signals per unit
803 area (2 x 2 cm) or per nucleus (n = 43) was quantified in **(B)** and **(C)**.
804 **(D and E)** BiFC analysis to detect interaction between STA1/sta1-1 and DOT2/dot2^{S}/dot2^{C}
805 under heat stress conditions in leaves of *N. benthamiana* (scale bar = 75 μm). Red arrows
806 indicate EYFP signals. EYFP signals were quantified from the same area of leaf disks (1 x 1
807 cm). Data are presented as means from three independent biological replicates. Statistical
808 analysis is performed using one-way ANOVA with Tukey's HSD test. Significant differences
809 are denoted by letters above the plots.
810 **(F and G)** Co-localization of EYFP signals from BiFC analysis of STA1/sta1-1 and
811 DOT2/dot2^{S}/dot2^{C} with the NS marker mRFP-U1-70K under heat stress conditions in leaves
812 of *N. benthamiana* (scale bar = 10 μm). Box plots show the number of NS exhibiting EYFP
813 signals. Center lines indicate medians; boxes represent interquartile range, and whiskers extend

814 to minimum and maximum values. For heat treatment, samples were incubated at 37°C for 1 h
815 in liquid MS medium following a 36 h post-infiltration incubation.
816

817 **Figure 5. Heat-sensitivity of *sta1-1* is restored to wild type levels in the *S307* suppressor**

818 **(A and B)** Heat survival test and quantification of survival rate of each plant genotype. Ten-
819 day-old plants of each genotype were exposed to heat stress (37°C for 48 h), and survived
820 plants were scored. Statistical analysis is performed using one-way ANOVA with Tukey's HSD
821 test ($^{**}P < 0.01$; $^{*}P < 0.05$; n.s., not significant).
822 **(C)** Assessment of pollen viability using Alexander staining (scale bar = 50 μm). Viable pollen
823 grains appear purple, while non-viable pollen grains are transparent. Red arrows indicate non-
824 viable pollen grains. Data are presented as means ± SE from three independent biological
825 replicates. Statistical analysis is performed using one-way ANOVA with Tukey's HSD test.
826 Significant differences are denoted by letters above the plots.
827

828 **Figure 6. Defective splicing of *HSFA1s* in *sta1-1* is rescued in *S307*, leading to proper**
829 **expression of downstream target genes**
830 **(A)** Heatmap showing the IR ratios in WT under heat stress (WT(H)), *sta1-1* under heat stress
831 (*sta1-1*(H)), and *S307* under heat stress (*S307*(H)). Each genotype is represented by three
832 independent biological replicates.
833 **(B)** Boxplot analysis showing IR ratio trends across genotypes for 67,103 transcripts exhibiting
834 significant changes in intron retention. Each box represents the IR ratio distribution for each
835 genotype, with lines connecting genotypes to indicate intron-specific changes. The ribbon
836 highlights the median and variability for visual summary, and the bold red line indicates the
837 overall trend of median IR ratios across genotypes. Median IR ratios for each genotype are
838 shown in parentheses. Statistical significance among genotypes was assessed using the
839 Kruskal–Wallis test followed by a post hoc Dunn's test with Benjamini–Hochberg correction.
840 Significant differences are denoted by letters above the plots.
841 **(C)** Changes in intron retention levels of transcripts in response to heat stress across different
842 genotypes. Paired notation denotes (number of introns/number of genes).
843 **(D)** Venn diagram showing transcripts with increased intron retention under heat stress in each

genotype.

(E and F) Quantification and validation of splicing defects in the master heat stress regulators *HSFA1*s. Box diagrams show spliced and unspliced isoforms. *PP2A* is used as a loading control. **(G)** qRT-PCR analysis of heat stress-related genes regulated by *HSFA1*s. The relative expression levels of each gene are shown in the graphs. Data are presented as mean ± SE from three independent biological replicates. Statistical analysis is performed using one-way ANOVA with Tukey's HSD test ($^{**}P < 0.01$; $^{*}P < 0.05$; n.s., not significant).

Figure 7. A proposed model for STA1-DOT2 interaction-mediated NS formation and pre-mRNA splicing in growth and heat stress responses

The STA1-DOT2 interaction, presumably reflecting the U4/U6·U5 tri-snRNP assembly, is important for NS formation. Proper NS formation ensures the production of correctly spliced transcripts required for normal growth and heat stress responses. The *sta1-1* mutation or heat stress weakens the STA1-DOT2 interaction, thereby reducing NS formation. This disrupted subnuclear localization of splicing components increases intron-retained transcripts, resulting in defective growth and heat stress responses.

862 **Supplemental Figure 1. Positional cloning and the identification of the *dot2^S* mutation in**
863 ***S307***
864 **(A)** Map of the *DOT2* locus on chromosome 5. Ninety-four F2 seedlings derived from an *S307*
865 x L*er* cross were used for mapping. The Simple sequence length polymorphism (SSLP)
866 markers used for mapping, Ch5_5.46Mb and Ch5_5.71Mb, are shown on the 184A1 and 35B3
867 BAC clones, respectively. Recombination numbers are shown under each marker locus.
868 **(B)** The mutation information of *dot2^S* mutation, including nucleotide and corresponding amino
869 acid changes.
870
871 **Supplemental Figure 2. Homologs and expression patterns of *DOT2*, a U4/U6·U5 tri-**
872 **snRNP associated protein**
873 **(A)** Multiple sequence alignment of DOT2 homologs.
874 **(B)** Expression patterns of *DOT2* and *STA1::GUS* in *Arabidopsis*. GUS signals are observed in
875 whole seedling, flower, silique, and trichome from left to right.
876
877 **Supplemental Figure 3. Phenotypes of the *dot2* single mutant alleles**
878 **(A)** Growth phenotypes of 3-week-old WT, *sta1-1*, *S307*, *dot2^S*, and *dot2^T* (SAIL_775_F10)
879 plants (scale bar = 5 cm).
880 **(B)** Splicing defects in marker genes across genotypes. Box diagrams show spliced and
881 unspliced isoforms. *PP2A* is used as a loading control.
882 **(C)** Representative confocal images of PI-stained root tips of 3-day-old WT, *sta1-1*, *S307*, *dot2^S*,
883 and *dot2^T* seedlings (scale bar = 25 μm). Arrowheads indicate dead cells, and white bars mark
884 the division zone. Division zone length in 3-day-old seedlings is quantified (n = 10). Statistical
885 analysis is performed using one-way ANOVA with Tukey's HSD test (**$P < 0.01$; n.s., not
886 significant).
887
888 **Supplemental Figure 4. Residue positions of mutations in sta1-1 and dot2 mutant proteins**
889 **(A)** Predicted protein structures of *Arabidopsis* STA1 and DOT2. In the model, STA1 protein
890 is shown in green and DOT2 protein in blue, with their respective mutations highlighted as
891 follows: the *sta1-1* mutation in magenta, the *dot2^S* mutation in red, and the *dot2^C* mutation in

892 orange.

893 **(B)** Domain structure of STA1 and DOT2. Predicted STA1-DOT2 interaction regions identified
894 using InterProSurf and PDBePISA are indicated by red lines (STA1: 113−123 aa, 185−202 aa;
895 DOT2: 548−569 aa). Domains are labeled as follows: UBQ, ubiquitin-like; PRP1P, pre−mRNA
896 processing protein 1; HAT, half-A-tetratricopeptide repeat; NLS, nuclear localization signal;
897 TPR, tetratricopeptide repeat; HIND, hub1−interacting domain.

898 **(C)** The *dot2*^{S} and *dot2*^{C} mutations, showing nucleotides and the corresponding amino acid
899 changes.

900 **(D)** Growth phenotypes of 3-week-old WT, *sta1-1*, *S307*, and the *sta1-1 dot2*^{C} double mutant
901 (*ssd*^{C}*d*^{C}) plants (scale bar = 5 cm).

902 **(E)** Splicing defects in the marker genes across genotypes. The box diagrams show spliced and
903 unspliced isoforms. *PP2A* is used as a loading control.

904

905 **Supplemental Figure 5. Rescue of *Salk007933* lethality through introduction of STA1-**
906 **GFP or sta1-1-GFP, resulting wild-type- and *sta1-1*-like phenotypes, respectively**

907 Growth phenotypes of 3-week-old *Salk007933*$^{STA1\text{-}GFP}$ and *Salk007933*$^{sta1\text{-}1\text{-}GFP}$ plants (scale
908 bar = 5 cm).

909

910 **Supplemental Figure 6. Increased STA1-aggregates under heat conditions**

911 **(A and B)** Subcellular localization of GFP-tagged STA1 and EYFP signals from BiFC analysis
912 of STA1-STA1 interaction under heat conditions (scale bar = 75 μm).

913 **(C and D)** Co-localization of EYFP signals from BiFC analysis of STA1-STA1 interaction
914 with the mRFP-U1-70K in leaves of *N. benthamiana* (scale bar = 10 μm).

915 **(E)** MolPhase prediction analysis of IDR region within STA1 (Liang *et al.*, 2024).

916 For heat treatment, samples were incubated at 37°C for 1 h in liquid MS medium following a
917 36 h post-infiltration incubation.

918

919 **Supplemental Figure 7. Intron-retained *HSFA1* transcripts in *sta1-1***

920 **(A)** Increased IR events of *HSFA1s* in *sta1-1* (H). IR events in *WT*(H), *sta1-1*(H), and *S307*(H)

921 are visualized using the Integrative Genomics Viewer (IGV).

922 **(B)** Protein domain structures of premature termination codon (PTC)-containing intron-
923 retained pre-mRNA isoforms in *sta1-1* (H). Domains are labeled as follows: DB, DNA-binding
924 domain; OD, oligomerization domain; NLS, nuclear localization signal; AHA1/2, aromatic and
925 large hydrophobic amino acid residues embedded in acidic surroundings. PTCs are labeled
926 with a red symbol.

927

928 **Supplemental Figure 8. Splicing defects of *HSFA1*s in *sta1-1 dot2^{C}* double mutants**

929 Splicing defects of the master heat stress regulators *HSFA1*s in the *sta1-1 dot2^{C}* double mutant
930 (*ssd^{C}d^{C}*) plants. Box diagrams show spliced and unspliced isoforms. *PP2A* is used as a loading
931 control.

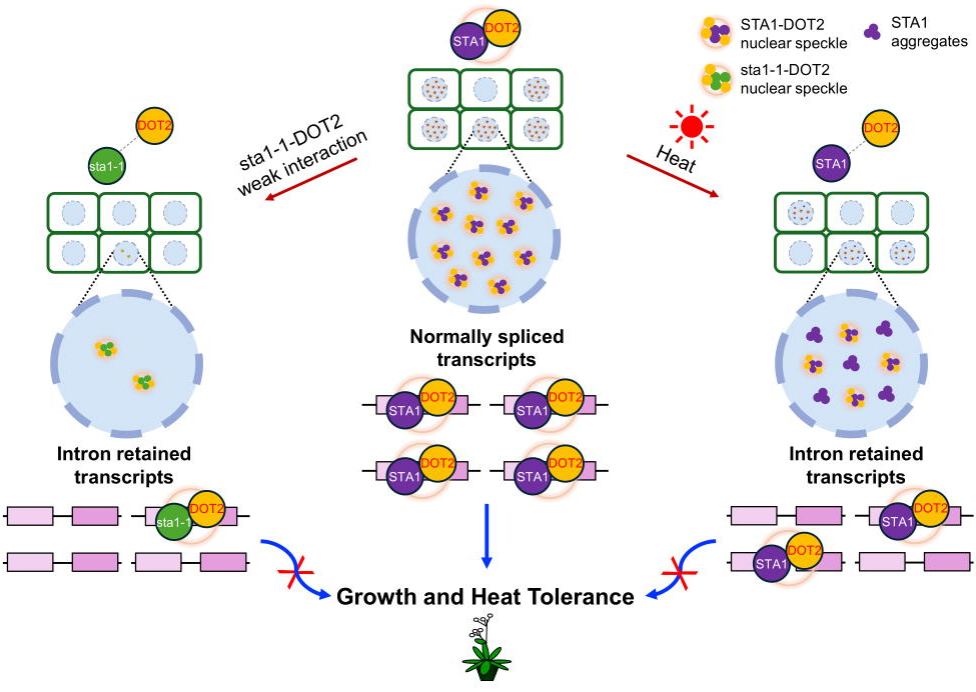
STA1-DOT2
nuclear speckle
STA1
aggregates
sta1-1-DOT2
nuclear speckle
sta1-1-DOT2
weak interaction
Heat
DOT2
sta1-1
STA1
Normally spliced
transcripts
Intron retained
transcripts
Intron retained
transcripts
Growth and Heat Tolerance

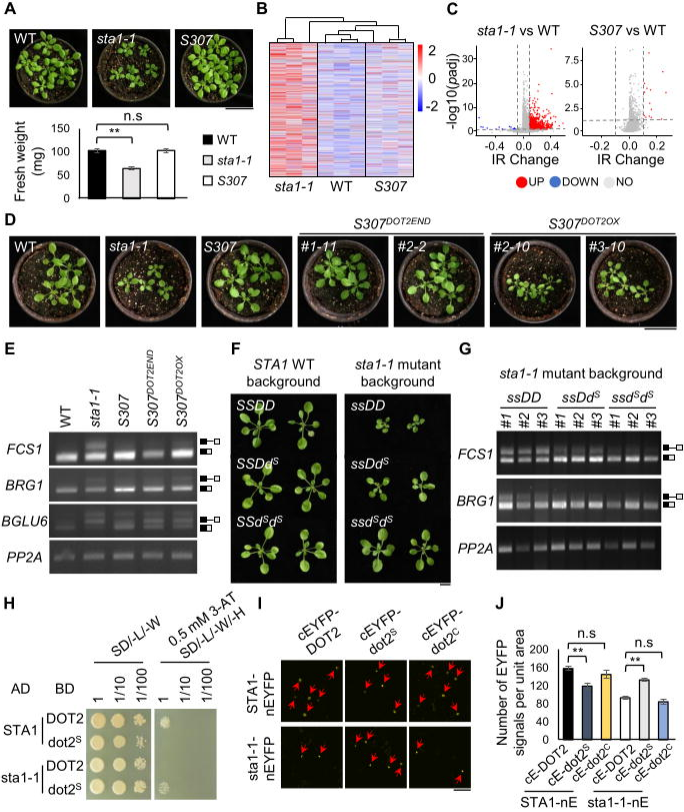
A
WT
sta1-1
S307
Fresh weight (mg)
150
100
50
0
n.s
**
WT
sta1-1
S307
B
2
0
-2
sta1-1
WT
S307
C
sta1-1 vs WT
S307 vs WT
-log10(padj)
30
20
10
0
7.5
5.0
2.5
-0.4
0.0
0.4
-0.2
0.0
0.2
IR Change
IR Change
UP
DOWN
NO
D
WT
sta1-1
S307
S307DOT2END
#1-11
#2-2
S307DOT2OX
#2-10
#3-10
E
WT
sta1-1
S307
S307DOT2END
S307DOT2OX
FCS1
BRG1
BGLU6
PP2A
F
STA1 WT background
sta1-1 mutant background
SSDD
SSDdS
SSdSdS
ssDD
ssDdS
ssdSdS
G
sta1-1 mutant background
ssDD
ssDdS
ssdSdS
#1
#2
#3
FCS1
BRG1
PP2A
H
SD/-L/-W
0.5 mM 3-AT SD/-L/-W/-H
AD
BD
1
1/10
1/100
STA1
DOT2
dot2S
sta1-1
DOT2
dot2S
I
cEYFP-DOT2
cEYFP-dot2S
cEYFP-dot2C
STA1-nEYFP
sta1-1-nEYFP
J
Number of EYFP signals per unit area
200
160
120
80
40
0
n.s
**
n.s
**
cE-DOT2
cE-dot2S
cE-dot2C
cE-DOT2
cE-dot2S
cE-dot2C
STA1-nE
sta1-1-nE

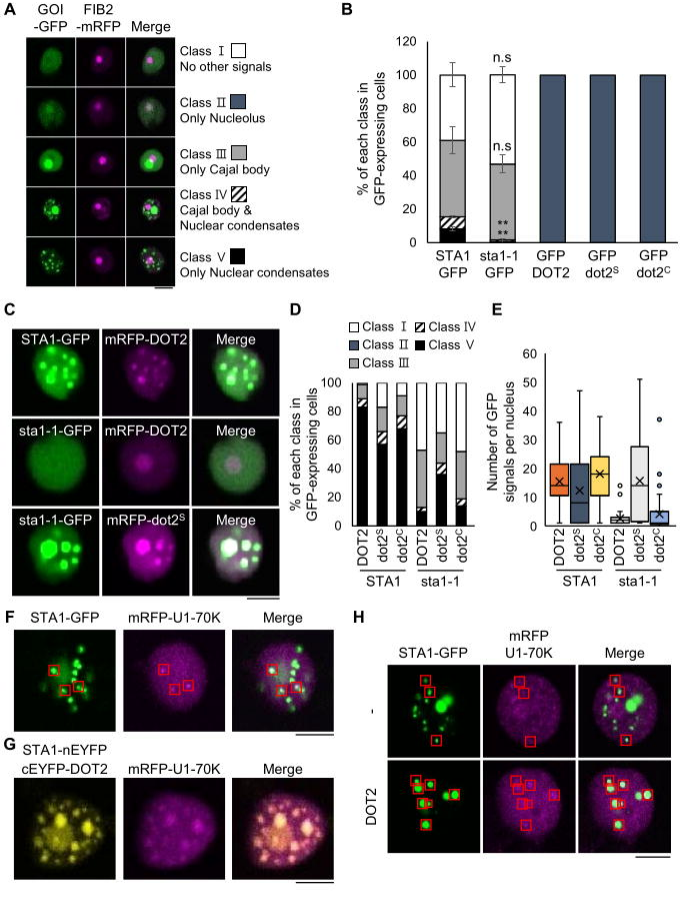
A
GOI -GFP
FIB2 -mRFP
Merge
Class Ⅰ No other signals
Class Ⅱ Only Nucleolus
Class Ⅲ Only Cajal body
Class Ⅳ Cajal body & Nuclear condensates
Class Ⅴ Only Nuclear condensates
B
% of each class in GFP-expressing cells
n.s
n.s
**
**
STA1 GFP
sta1-1 GFP
GFP DOT2
GFP dot2S
GFP dot2C
C
STA1-GFP
mRFP-DOT2
Merge
sta1-1-GFP
mRFP-DOT2
Merge
sta1-1-GFP
mRFP-dot2S
Merge
D
Class Ⅰ
Class Ⅱ
Class Ⅲ
Class Ⅳ
Class Ⅴ
% of each class in GFP-expressing cells
DOT2
dot2S
dot2C
STA1
sta1-1
E
Number of GFP signals per nucleus
F
STA1-GFP
mRFP-U1-70K
Merge
G
STA1-nEYFP
cEYFP-DOT2
mRFP-U1-70K
Merge
H
STA1-GFP
mRFP U1-70K
Merge
-
DOT2

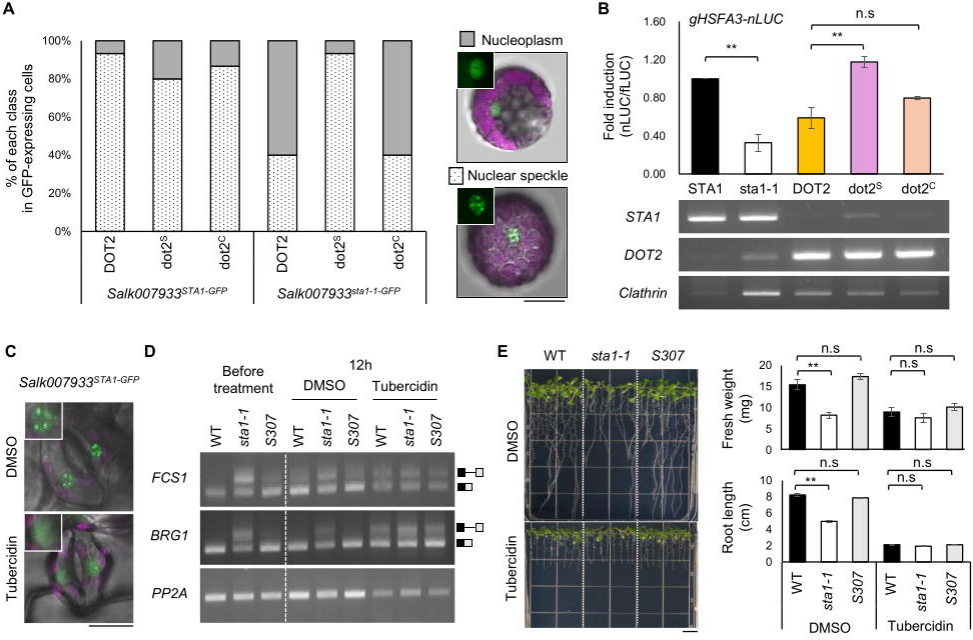
A
100%
80%
60%
40%
20%
0%
% of each class in GFP-expressing cells
DOT2
dot2S
dot2C
DOT2
dot2S
dot2C
Salk007933STA1-GFP
Salk007933sta1-1-GFP
Nucleoplasm
Nuclear speckle
B
gHSFA3-nLUC
Fold induction (nLUC/fLUC)
1.60
1.20
0.80
0.40
0.00
**
**
n.s
STA1
sta1-1
DOT2
dot2S
dot2C
STA1
DOT2
Clathrin
C
Salk007933STA1-GFP
DMSO
Tubercidin
D
Before treatment
12h
DMSO
Tubercidin
WT
sta1-1
S307
FCS1
BRG1
PP2A
E
WT
sta1-1
S307
DMSO
Tubercidin
Fresh weight (mg)
Root length (cm)
n.s
**
DMSO
Tubercidin

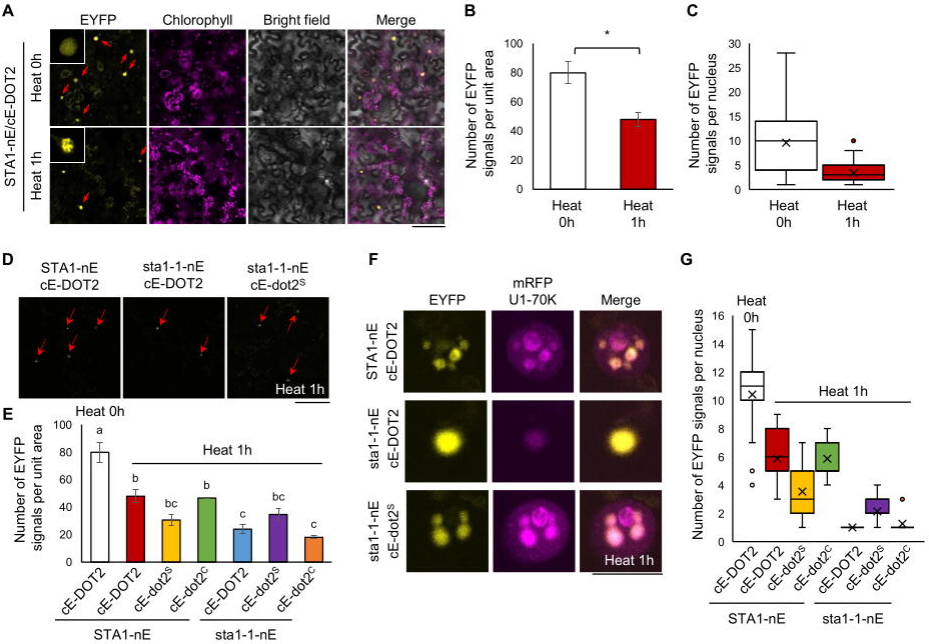
A
EYFP
Chlorophyll
Bright field
Merge
STA1-nE/cE-DOT2
Heat 0h
Heat 1h
B
Number of EYFP signals per unit area
100
80
60
40
20
0
*
Heat 0h
Heat 1h
C
Number of EYFP signals per nucleus
30
25
20
15
10
5
0
Heat 0h
Heat 1h
D
STA1-nE cE-DOT2
sta1-1-nE cE-DOT2
sta1-1-nE cE-dot2S
Heat 1h
E
Heat 0h
Heat 1h
Number of EYFP signals per unit area
a
b
bc
b
c
bc
c
cE-DOT2
cE-DOT2
cE-dot2S
cE-dot2C
cE-DOT2
cE-dot2S
cE-dot2C
STA1-nE
sta1-1-nE
F
EYFP
mRFP U1-70K
Merge
STA1-nE cE-DOT2
sta1-1-nE cE-DOT2
sta1-1-nE cE-dot2S
Heat 1h
G
Heat 0h
Heat 1h
Number of EYFP signals per nucleus
16
14
12
10
8
6
4
2
0
cE-DOT2
cE-DOT2
cE-dot2S
cE-dot2C
cE-DOT2
cE-dot2S
cE-dot2C
STA1-nE
sta1-1-nE

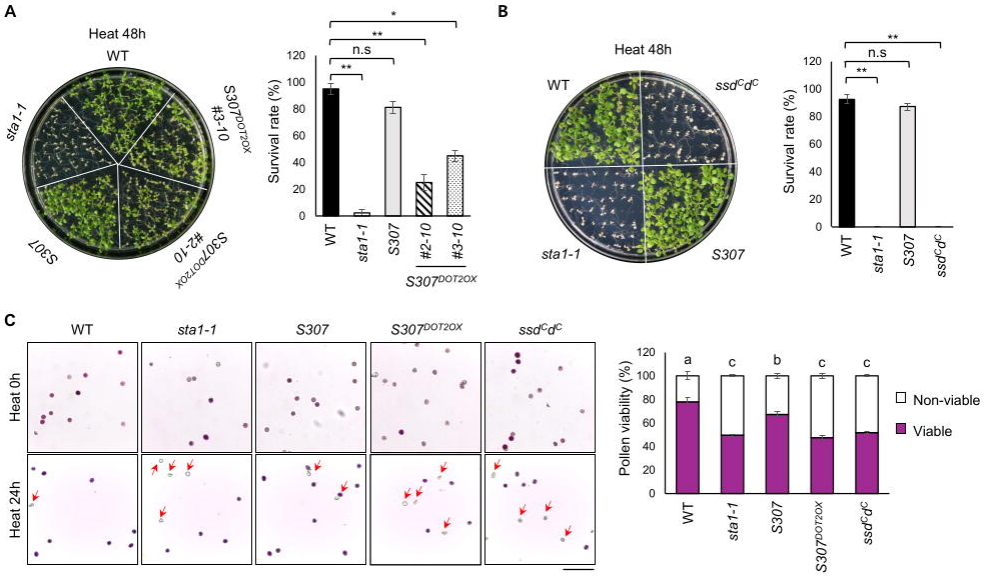
A
Heat 48h
WT
sta1-1
S307DOT2OX #3-10
S307DOT2OX #2-10
S307
Survival rate (%)
120
100
80
60
40
20
0
n.s
**
*
WT
sta1-1
S307
#2-10
#3-10
S307DOT2OX
B
Heat 48h
WT
ssdCdC
sta1-1
S307
Survival rate (%)
n.s
**
WT
sta1-1
S307
ssdCdC
C
WT
sta1-1
S307
S307DOT2OX
ssdCdC
Heat 0h
Heat 24h
Pollen viability (%)
a
c
b
c
c
Non-viable
Viable
WT
sta1-1
S307
S307DOT2OX
ssdCdC

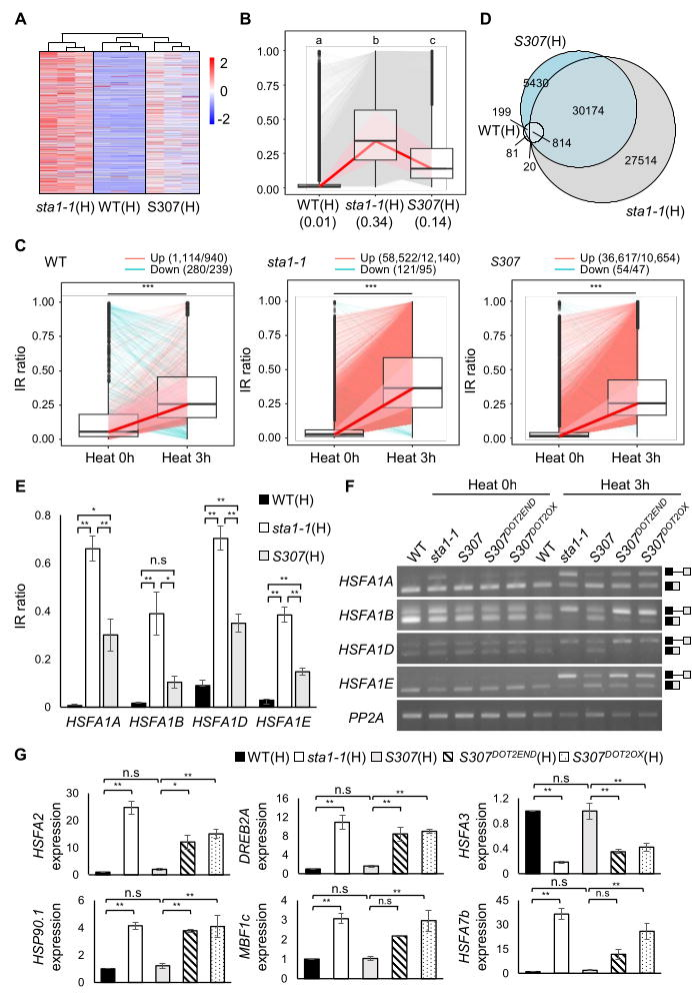
A
2
0
-2
sta1-1(H) WT(H) S307(H)
B
a
b
c
1.00
0.75
0.50
0.25
0.00
WT(H) sta1-1(H) S307(H)
(0.01) (0.34) (0.14)
D
S307(H)
5438
30174
199
WT(H)
814
81
20
27514
sta1-1(H)
C
WT
Up (1,114/940)
Down (280/239)
sta1-1
Up (58,522/12,140)
Down (121/95)
S307
Up (36,617/10,654)
Down (54/47)
***
IR ratio
Heat 0h
Heat 3h
E
WT(H)
sta1-1(H)
S307(H)
IR ratio
n.s
HSFA1A HSFA1B HSFA1D HSFA1E
F
Heat 0h
Heat 3h
WT sta1-1 S307 S307DOT2END S307DOT2OX WT sta1-1 S307 S307DOT2END S307DOT2OX
HSFA1A
HSFA1B
HSFA1D
HSFA1E
PP2A
G
WT(H) sta1-1(H) S307(H) S307DOT2END(H) S307DOT2OX(H)
HSFA2 expression
DREB2A expression
HSFA3 expression
HSP90.1 expression
MBF1c expression
HSFA7b expression
n.s